Simultaneous large mode index and high quality factor in infrared hyperbolic metamaterials

Patrick Sohr,[1†] Dongxia Wei,[1†] Stephanie Tomasulo,[2] Michael K. Yakes,[2] and Stephanie Law[1*]

[1] Department of Materials Science and Engineering, University of Delaware, Newark, Delaware 19702, United States

[2] Naval Research Laboratory, 4555 Overlook Ave. SW, Washington, DC 20375, United States

[*]corresponding author: slaw@udel.edu

[†] Patrick Sohr and Dongxia Wei contributed equally

Abstract

Semiconductor hyperbolic metamaterials comprise alternating doped (metal) and undoped (dielectric) subwavelength semiconductor layers. These materials support high wavevector modes called volume plasmon polaritons. Here, we investigate the quality and modal indices of volume plasmon polaritons in three semiconductor systems: Si:InGaAs/InAlAs, Si:InAs/GaSb, and Si:InAs/AlSb. We are able to demonstrate modal indices as high as 15, which is higher than any other artificial hyperbolic metamaterial within its respective wavelength range. We achieve this while maintaining quality factors as high as 14, comparable to those same material systems. Understanding of how the material combinations of these semiconductor hyperbolic metamaterials affect the volume plasmon polaritons provides the groundwork for the development of tunable, low-loss, infrared optoelectronic devices.

Key Words: hyperbolic metamaterial, semiconductor metamaterial, volume plasmon polariton

The ability to create materials and heterostructures with designer permittivity profiles is fundamental to advances in optics, optoelectronics, and nanophotonics. Control over the permittivity results in precise control over the flow of light within a structure. Hyperbolic materials are those that show a positive permittivity along one axis and a negative permittivity along the other over some bandwidth. These materials have an open, hyperbolic isofrequency surface, leading to a large photonic density of states[1–4]. This leads to a variety of unusual optical phenomena, including negative group velocity, large effective index of refraction, and slow light[5,6]. Applications for hyperbolic materials include imaging subwavelength features, increasing the radiative recombination rate of emitters, subwavelength waveguiding, and more[1,3,7,8]. Unfortunately, naturally hyperbolic materials tend to show hyperbolic behavior over a relatively narrow bandwidth with an optical response dictated by the inherent material properties[9–11]. Alternatively, we can turn to artificially engineered hyperbolic metamaterials (HMMs). These composite materials can be created by stacking alternating subwavelength layers of metal and dielectric, resulting in a structure that can be treated as an effective medium with different permittivities in the direction parallel to the layers ($\varepsilon_{\parallel}$) and perpendicular to the layers ($\varepsilon_{\perp}$). Unlike natural hyperbolic materials, the properties of an HMM can be tuned by adjusting the permittivities of the metal and dielectric, the individual layer thicknesses, or the fill factor (ratio of metal thickness to metal and dielectric thickness).

The open isofrequency surface found in all materials with hyperbolic dispersion means that electromagnetic waves with arbitrarily large wavevectors can propagate in the material. These large wavevector modes are called volume plasmon polaritons (VPPs) and are leveraged in the subwavelength imaging, environmental sensing, subwavelength diffraction, and waveguiding applications described earlier. In layered HMMs, VPPs arise from the coupling of surface plasmon polaritons (SPP) at every metal/dielectric interface, leading to complex optical modes with large modal indices[12–14]. Understanding the properties of these VPP modes and how they depend on material parameters is crucial for the development of new devices that harness these modes. VPPs have already been studied in HMMs fabricated from a variety of materials, including gold, TiO_2, SiO_2, Al_2O_3 and Si[15–19]. Unfortunately, these materials are not infrared-compatible, and it is difficult to embed other optoelectronic device components inside these HMMs. Heavily-doped III-V semiconductors have been shown to act as infrared plasmonic metals whose optical properties can be tuned by changing the doping density[20,21]. Growing structures with alternating doped (metallic) and undoped (dielectric) semiconductor layers can easily be done using molecular beam epitaxy (MBE), which provides structures with atomically-sharp interfaces, low defect densities, and good crystal quality[22,23]. One of the major advantages of semiconductor HMMs over other hyperbolic materials is the ability to epitaxially embed other semiconductor optoelectronic components, like quantum wells and quantum dots, during the growth to create complex optoelectronic devices that harness the unique properties of the HMM[24].

In this paper, we excite up to five orders of VPP modes in HMMs fabricated from three different metal/dielectric material classes: Si:InGaAs/InAlAs, Si:InAs/GaSb, and Si:InAs/AlSb. We show that these modes span the long-wave infrared with quality factors as high as 14, effective mode indices reaching 15, and coupling efficiency into the modes approaching unity. The strong in-coupling is created by an efficient metallic grating coupler. The modal indices of VPPs created from other materials for the visible and near-IR vary from about 1 to 9 with quality factors similar to those reported here[15–19]. Semiconductor HMMs can therefore demonstrate strong light confinement while maintaining reasonable losses. The high quality of the VPP modes combined with the efficient grating coupler for either in- or out-coupling paves the way for the design of complex HMM devices with embedded emitter and detector structures.

The three samples discussed in this paper were grown using MBE. The Si:InAs/AlSb and Si:InAs/GaSb samples were grown on undoped GaAs wafers using the interfacial misfit technique to quickly relax the strain between the GaAs substrate and the AlSb or GaSb layers. The lattice-matched Si:$In_{0.53}Ga_{0.47}As/In_{0.52}Al_{0.48}As$ was grown on a Fe:InP wafer. In all cases, a single metal or dielectric layer was approximately 100nm. All structures have 10 periods, resulting in a HMM with a total thickness around 2μm. The electron density in the doped metallic layers was chosen such that the plasma wavelength of those layers was between 8-9μm. Each structure ended with an undoped dielectric layer. Further details of the growth can be found in[21,23,25]. Theoretical treatment discussing the metallic behavior of the doped semiconductor layer and the effective medium treatment of the HMM can be found in the Supporting Information.

The VPP modes necessarily have a much larger wavevector than the incident light, so a grating coupler was fabricated on top of the samples to enable excitation of the VPP modes. Since the top layer for each of the samples is an undoped semiconductor, the grating is separated from the first HMM metal layer by 100nm. After fabrication, TM- and TE-polarized reflection spectra were obtained using Fourier transform infrared spectroscopy. The reflection spectra for the unpatterned samples were modeled using a T-matrix Mathematica program to confirm the plasma wavelength and scattering rate of the grown samples. Details of this fitting procedure can be found in the references[23,26]. Patterned samples were simulated by finite element analysis using Comsol Multiphysics 5.3. NextNano, a self-consistent Poisson solver, was used to determine the electron distribution at the interface of the metal and dielectric layers using known band offsets.

Results and Discussion

In Figs. 1(a-c), we plot the TM-polarized reflection spectra for all three samples. The plots start after the topological transition point between the type I and type II HMMs regimes. The plots cut off at 28μm due to limitations of our measurement setup. Each sample was cleaved into multiple smaller pieces, so gratings of different periods could be fabricated. This enables us to excite multiple VPP modes and map out their dispersion on identical chips. Fig. 1(a) shows reflection spectra for the Si:InGaAs/InAlAs sample. We observe three VPP modes with moderate linewidth and moderate intensity. As we move to Figs. 1(b) and (c), we see three VPP modes (for the Si:InAs/GaSb sample) then five modes (for the Si:InAs/AlSb sample). These modes also become narrower and stronger. In some of the curves, some weaker intensity modes are observed. These modes are reproduced in theoretical modeling and are discussed in detail in the Supporting Information.

To understand the difference in VPP behavior for the three different samples, we first consider the electron distribution in the samples. Figs. 1(d-f) show the electron distribution as a function of depth in all three samples, calculated using NextNano. The maximum electron concentration in these three samples varies slightly due to difference in silicon dopant flux and incorporation during growth. An ideal HMM will have a perfect square-wave profile, in which all the electrons are confined to the metallic layers, leaving the dielectric layers completely undoped. This type of profile is observed only in the Si:InAs/AlSb sample, shown in Fig. 1(f), and arises from the large conduction band offset between InAs and AlSb. The Si:InAs/GaSb sample also shows good confinement, though there is a small rounded shoulder at the InAs/GaSb interface. This is likely due to the smaller band offset as well as the type III band alignment, which leads to band bending at the interface and a concomitant reduction in electron density. The Si:InGaAs/InAlAs likewise has acceptable carrier confinement, though shoulders exist on both sides of the interface due to the smaller conduction band offset.

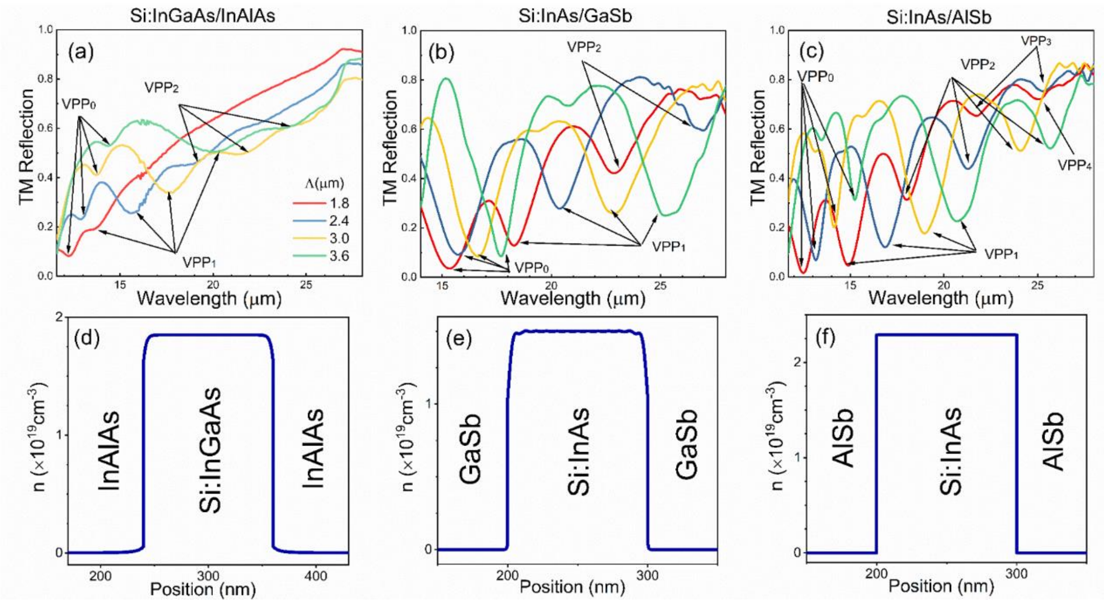

Figure 1: Experimental TM reflection of samples with varying grating period and simulated carrier distribution as a function of sample depth.

As mentioned previously, VPP modes originate from the coupling of SPPs at each dielectric/metal interface. A sharp interface indicates a single value of carrier density on the metal side. This results in a sharp SPP resonance at the interface. A graded interface indicates a depth-dependent carrier density, leading to a broader, weaker SPP resonance as described previously[26]. The Si:InAs/AlSb sample has the largest carrier confinement and shows the most VPP modes with the highest quality. The Si:InGaAs/InAlAs and the Si:InAs/GaSb samples have conduction band offsets and electron profiles similar to one another, but vastly different VPP mode properties. This can be understood by considering the influence of alloy scattering. Ternary compounds like InGaAs and InAlAs have an additional scattering pathway due to the random nature of the ternary alloy. Alloy scattering has been demonstrated to be a significant scattering pathway for InGaAs/InAlAs two-dimensional electron gasses[27,28]. The two-dimensional confined nature of the SPPs makes it likely that alloy scattering contributes to the broadening and weakening of the VPP modes in these samples.

We now turn our attention to the properties of the VPP modes themselves. We begin by explaining the mode indexing scheme used in this paper. It is based on schemes proposed by Avrutsky et al[12]. The VPP modes are identified by their number of nodes in the magnetic field in the z-direction: the first VPP mode, VPP0, has zero nodes, and the number of nodes increases for each subsequent higher order mode. In Fig. 2(a), we plot the magnetic field profiles extracted from modeling the Si:InAs/AlSb HMM with a 1.8μm grating period. There is a noticeable decrease in the intensity of the magnetic field as the mode index increases, which is consistent with the experimental observation of a decrease in VPP mode strength with increasing index. We will discuss this in detail later. Fig. 2(b) takes a vertical line profile through the center of sample at each of the VPP modes, and the number of nodes can be seen clearly. For a sample with identical cladding layers, we would expect the VPP modes to be symmetric in both the vertical and horizontal directions. However, our samples are grown on GaAs substrates (refractive index n~3.3) and have air as a top cladding (n=1) with a gold grating coupler. We therefore observe significant vertical asymmetry in the field profiles. The asymmetry is caused both by the difference in refractive indices as well as the effects of the gold grating coupler, which both in-couples the light and allows the VPP modes to scatter back into free space.

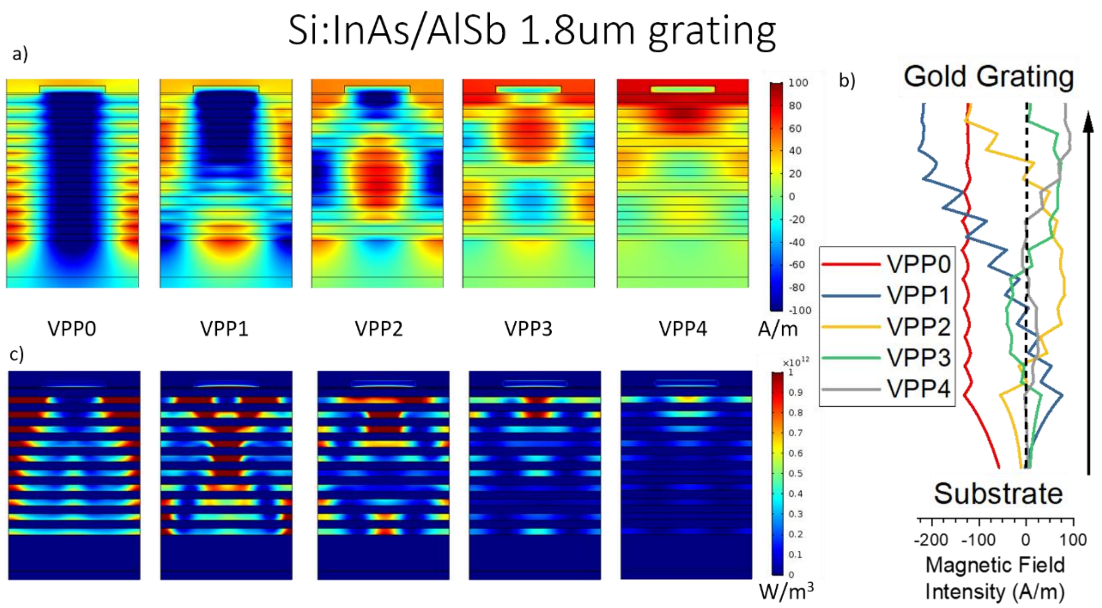

Figure 2: (a) Magnetic field profiles for the five VPP modes for the Si:InAs/AlSb HMM with a 1.8μm grating. (b) The magnetic field intensity as a function of vertical position through the sample. The black dashed line indicates the zero point, and the sawtooth nature of the lines are the result of the alternating metal and dielectric layers. (c) Resistive heating profiles for the five VPP modes for the Si:InAs/AlSb HMM as shown in part (a).

Many of the proposed applications for semiconductor HMMs leverage these VPP modes and require the modes to be both low loss and exhibit large effective indices. For example, subwavelength imaging using hyperlenses requires VPP modes with large index to carry the subwavelength information about the object through the hyperlens with low losses. To determine the best material system for a given application, we need to investigate the losses, quality factor, and effective index of the modes. These parameters can be extracted from the raw data presented in Figs. 1(a-c). The data were fitted with multiple Lorentzian oscillators, and the position and full width half maximum (FWHM) were extracted for each mode. The quality factor is given by the resonance wavelength divided by the FWHM, while the effective index is given by the ratio of the wavevector in the material to the wavevector in free space. It should be noted that the number of visible modes is generally related to the mode quality; more, higher-order modes will be visible in lower-loss systems. In an ideal system, the number of modes is equal to the number of dielectric layers within the structure. As such, we would expect to be able to observe nine VPP modes. The maximum number of modes we observe is five in the Si:InAs/AlSb sample with a grating period of 1.8μm. This limit is due to the 30μm cutoff wavelength of our polarizer and beamsplitter. Therefore, it is not a direct measure of the quality of the samples. The dispersion of VPP0 is shown in Fig. S2 in the Supporting Information and compared with theory; a good match is observed.

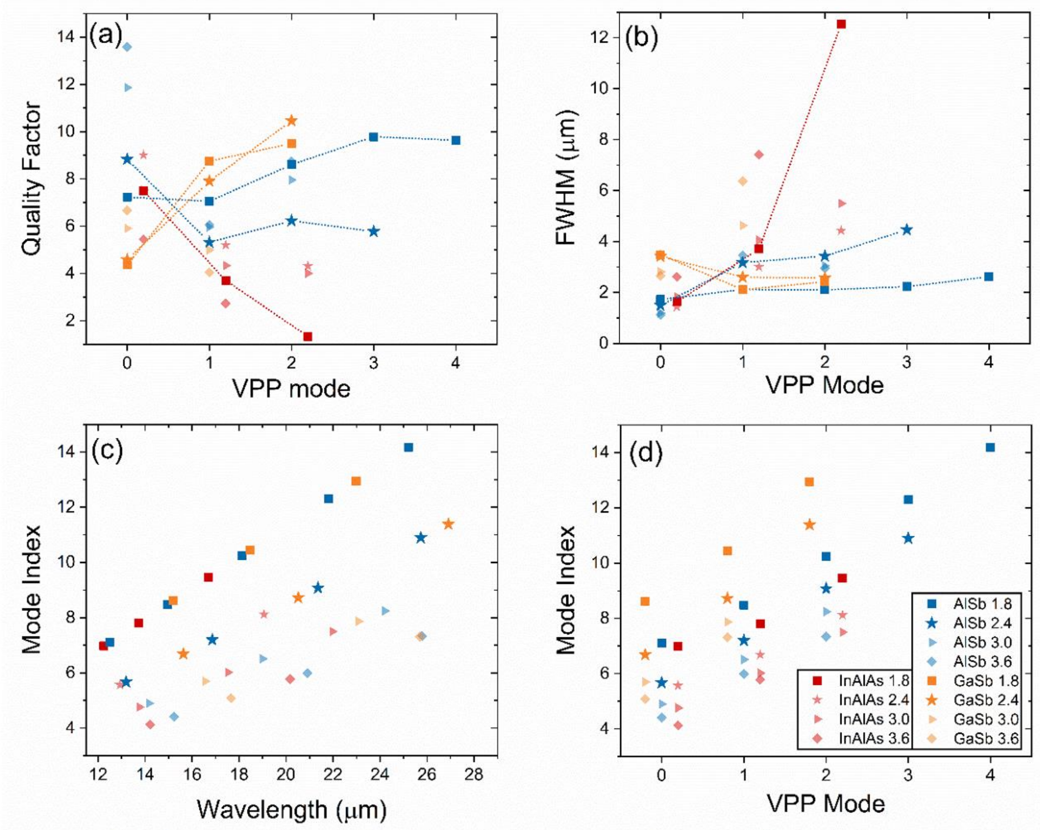

Figure 3: (a) Quality factor as a function of mode number, (b) FWHM as a function of mode number, (c) mode index as a function of wavelength, and (d) mode index as a function of mode number for each VPP mode for all three materials and all four grating periods, as indicated in the legend. In (a), (b), and (d) some of the points are offset horizontally for clarity.

In Fig. 3, we show the results of the analysis of the VPP modes. Theoretical work indicates that the losses and mode index should both increase with mode order[12]. This can be understood by realizing that as the mode order increases, light is being squeezed into a smaller volume. Better confinement generally corresponds to higher losses, leading to smaller quality factors. Fig. 3(a) plots the quality factor for all modes as a function of VPP mode order. Focusing on the data for the 1.8μm grating on the Si:InGaAs/InAlAs sample (red squares), we see that the quality factor decreases as the mode order increases. This trend is reproduced for all the Si:InGaAs/InAlAs samples.

In Figs. 3(b) and (d), we see the FWHM and the mode index for the Si:InGaAs/InAlAs increasing with VPP mode order, leading to an overall decrease in quality factor. This trend matches the theory. This material system shows generally low quality factors (Q<8) and modest mode indices (n^*<10). We attribute the comparatively worse behavior of this system to the alloy scattering described previously, which amplifies the losses from the increased confinement.

The Si:InAs/AlSb and Si:InAs/GaSb samples behave somewhat unexpectedly, as highlighted with the blue and orange squares and stars. For both cases, the mode index monotonically increases with mode number, as expected. However, the FWHM for all of the Si:InAs/AlSb samples stays relatively constant with mode index, showing only a small increase which can be observed for the representative highlighted samples. This leads to quality factors that are relatively constant with mode index, generally showing only small decreases or slight increases. The FWHM for the two highlighted Si:InAs/GaSb samples (the 1.8μm and 2.4μm gratings) actually decreases with mode index, though the two other samples (for which only two data points exist) show increases in FWHM with mode index. This behavior suggests that the dominant loss pathways for the Si:InAs/AlSb and the Si:InAs/GaSb samples cannot just be described by a single, unvarying number that is constant throughout the material. To understand these results, we can plot the FWHM as a function of wavelength, as shown in Fig. 4. Each VPP mode is marked with a different color, to highlight how the FWHM changes for a given mode as a function of wavelength. Fig. 4(a) shows the data for the Si:InGaAs/InAlAs sample. Generally, the FWHM for a given mode increases as the mode resonance shifts to longer wavelengths, with VPP2 at ~17μm standing out as a clear exception. For the Si:InAs/GaSb and Si:InAs/AlSb samples, however, we see different behavior. In both of these cases, the FWHM of VPP0 decreases as it moves to longer wavelengths. The other VPP modes for both Si:InAs/GaSb and Si:InAs/AlSb generally show an increase in FWHM as the wavelength increases.

The behavior of the FWHMs of the VPP modes can generally be described by considering the imaginary part of the effective parallel ($\varepsilon_\parallel''$) and perpendicular ($\varepsilon_\perp''$) permittivities of the HMM. For a layered semiconductor HMM like the ones described here, the material will behave like a dielectric in both the parallel and perpendicular directions for wavelengths shorter than the plasma wavelength of the metallic layers. As the wavelength increases, the material enters the type I HMM regime, in which the real part of the effective perpendicular permittivity ($\varepsilon_\perp'$) is negative, while the real part of the effective parallel permittivity ($\varepsilon_\parallel'$) is positive. As the wavelength continues to increase, the material transitions into the type II HMM regime, where the signs of the real parts of the permittivities are reversed. This is the regime in which we observe VPP modes. The transition from type I to type II HMM is accompanied by a large increase in $\varepsilon_\perp''$. As the wavelength increases beyond the type I to type II transition, $\varepsilon_\perp''$ is larger than $\varepsilon_\parallel''$, but decreasing rapidly. At the same time, $\varepsilon_\parallel''$ is slowly increasing. Eventually these two curves cross and $\varepsilon_\parallel''$ is larger than $\varepsilon_\perp''$ and continues to increase with increasing wavelength (curves are shown in Fig. S1 in the Supplementary information). Overall, the imaginary part of the permittivity initially rapidly decreases after the transition from type I to type II behavior, then slowly begins increasing again. This behavior can be exactly mapped to the FWHM of the VPP modes. The vertical dotted line on the plots in Fig. 4 indicates this crossover point. We can see that the points to the left of this line generally show decreasing FWHM as the wavelength increases, while points to the right side of the line show the opposite behavior. The Si:InAs/GaSb sample is particularly well-described with this model. The Si:InGaAs/InAlAs behavior can be attributed to a FWHM "floor" due to the alloy scattering. This sets a lower limit on the FWHM regardless of any other factors in the system and explains why this sample does not follow this trend. It is currently unclear why the shortest wavelength VPP2 mode for the Si:InGaAs/InAlAs system shows such a large FWHM.

Finally, to completely describe the system we must also consider why the VPP1 mode for the Si:InAs/AlSb sample always shows a higher FWHM than we would expect. There are a number of factors influencing this mode. The first is the existence of as yet unidentified resonances in this system near the resonant wavelength of VPP1. These can be observed as small dips in the reflection spectra shown in Fig. 1(c) that are not identified as VPP modes but are reproduced in the modeling. The magnetic field profiles for these modes are shown in Fig. S3 in the Supplementary Information. It is possible that an interaction between these modes and VPP1 are leading to an artificial increase in the FWHM. We can also consider the resistive heating map of VPP1, as shown in Fig. 2(c). Compared to the other VPP modes, VPP1 has the largest resistive heating near the HMM/substrate interface. AlSb exhibits an approximately 7% lattice mismatch with the GaAs substrate. Although the interfacial misfit technique was used to quickly relax the strain between the GaAs substrate and the AlSb layers, any residual strain or threading dislocations will predominantly affect these first few layers[29]. This lattice mismatch also exists in the Si:InAs/GaSb samples, but it is possible that these samples have higher quality than the Si:InAs/AlSb samples. Lower material quality at the film/substrate interface could therefore lead to larger FWHMs than predicted for VPP1 due to the mode profile. This result implies that the VPP modes could be used as a way of determining HMM material quality even at buried interfaces.

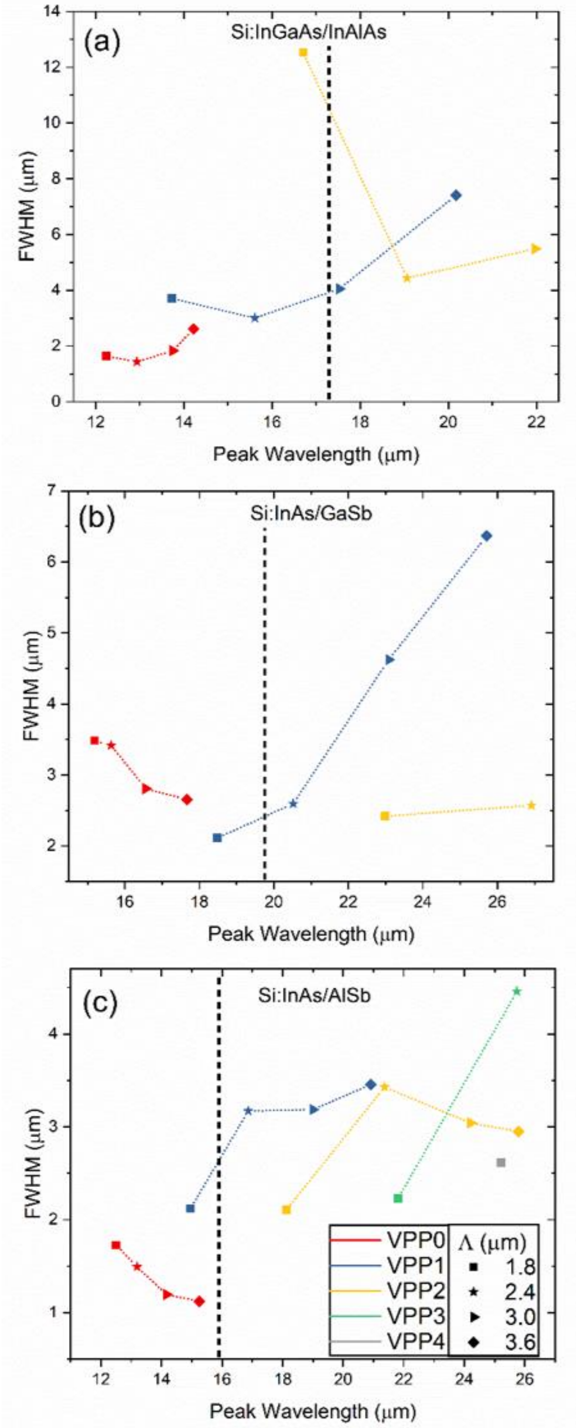

Figure 4: FWHM for all VPP modes for the (a) Si:InGaAs/InAlAs system, (b) Si:InAs/GaSb system, and (c) Si:InAs/AlSb system. The dotted vertical line indicates where $\varepsilon''_{\parallel}$ becomes larger than $\varepsilon''_{\perp}$.

Our work demonstrates that the properties of semiconductor-based HMMs are promising for a variety of applications in the infrared. Within the Si:InAs/AlSb system, we observe quality factors as high as 15, which is comparable to values observed in visible-wavelength HMMs and other semiconductor metamaterial resonators[15–19]. The highest mode index obtained in this system is 14 with a quality factor of 9.6. This is the highest mode index reported in an artificial hyperbolic metamaterial of any type. In addition, the ability to design structures with an engineered permittivity as well as the ability to epitaxially embed other semiconductor optoelectronic device components makes these artificial HMMs extremely promising for infrared emitter and detector components. Now that we have a better understanding of the behavior of the large-wavevector VPP modes in semiconductor HMMs, we can begin to design complex devices to control the flow of infrared light at the subwavelength scale.

Methods

Fabrication: Ti/Au gratings were fabricated on the surfaces of all three HMMs with period ranging from 1.8μm-3.6μm with a stripe width of half the period. The gratings were made using standard electron-beam lithography, electron-beam deposition, and liftoff techniques. The thickness of the gold layer is 100nm with a 15nm titanium adhesion layer on the bottom. Since the top layer for each of the samples is an undoped semiconductor, the grating is separated from the first HMM metal layer by 100nm.

Spectroscopy: Spectra were taken using a Bruker Vertex 70V Fourier transform infrared (FTIR) spectrometer. Polarization- and angle-dependent reflection spectra were acquired for unpatterned samples from 25-80 degrees using an external setup with a KBr beamsplitter, a KRS-5 holographic wire grid polarizer, and a MCT detector. Transverse electric (TE) and transverse magnetic (TM) reflection spectra were acquired for the patterned samples at a 10-degree incident angle in the vacuum space of the FTIR using a Pike 10Spec accessory and the internal wide-range DTGS detector. For all cases, the data is normalized to polarized reflection spectra from a gold mirror.

Modeling: The reflection spectra for the unpatterned samples were modeled using a T-matrix Mathematica program and assuming the effective medium theory is appropriate. Details of this fitting procedure can be found in the references[23,26]. Patterned samples were simulated by finite element analysis using Comsol Multiphysics 5.3. The model was built to simulate the reflection of the patterned HMMs at a 10-degree incident angle under both TE and TM polarizations. The optical properties of the doped layers of the HMM were modeled using a Drude-Lorentz dispersion model, while the permittivity of the dielectric was assumed to be a constant over this range of wavelengths. The plasma wavelengths, metal/dielectric filling ratio, and scattering rates were determined as discussed above. NextNano, a commercially-available self-consistent Poisson solver, was used to determine the electron distribution at the interface of the metal and dielectric layers using known band offsets.

Supporting information

Expression for permittivity of doped semiconductor and effective medium theory, dispersion of volume plasmon polariton modes, and discussion of unknown modes.

Acknowledgments

This material is based upon work supported by the National Science Foundation under

Grant No. 1606673 and the Office of Naval Research.

References

(1) Liu, Z.; Lee, H.; Xiong, Y.; Sun, C.; Zhang, X. Far-Field Optical Hyperlens Magnifying Sub-Diffraction-Limited Objects. *Science* **2007**, *315*, 1686.

(2) Yao, J.; Wang, Y.; Tsai, K. T.; Liu, Z.; Yin, X.; Bartal, G.; Stacy, A. M.; Wang, Y. L.; Zhang, X. Design, Fabrication and Characterization of Indefinite Metamaterials of Nanowires. *Philos. Trans. R. Soc. A* **2011**, *369*, 3434–3446.

(3) Jacob, Z.; Smolyaninov, I. I.; Narimanov, E. E. Broadband Purcell Effect: Radiative Decay Engineering with Metamaterials. *Appl. Phys. Lett.* **2012**, *100*, 181105.

(4) Jacob, Z.; Kim, J.-Y.; Naik, G. V.; Boltasseva, A.; Narimanov, E. E.; Shalaev, V. M. Engineering Photonic Density of States Using Metamaterials. *Appl. Phys. B* **2010**, *100*, 215–218.

(5) Ji, D.; Song, H.; Zeng, X.; Hu, H.; Liu, K.; Zhang, N.; Gan, Q. Broadband Absorption Engineering of Hyperbolic Metafilm Patterns. *Sci. Rep.* **2014**, *4*, 4498.

(6) Cui, Y.; Fung, K. H.; Xu, J.; Ma, H.; Jin, Y.; He, S.; Fang, N. X. Ultrabroadband Light Absorption by a Sawtooth Anisotropic Metamaterial Slab. *Nano Lett.* **2012**, *12*, 1443–1447.

(7) Rho, J.; Ye, Z.; Xiong, Y.; Yin, X.; Liu, Z.; Choi, H.; Bartal, G.; Zhang, X. Spherical Hyperlens for Two-Dimensional Sub-Diffractional Imaging at Visible Frequencies. *Nat. Commun.* **2010**, *1*, 143.

(8) Noginov, M. A.; Li, H.; Barnakov, Y. A.; Dryden, D.; Nataraj, G.; Zhu, G.; Bonner, C. E.; Mayy, M.; Jacob, Z.; Narimanov, E. E. Controlling Spontaneous Emission with Metamaterials. *Opt. Lett.* **2010**, *35*, 1863–1865.

(9) Caldwell, J. D.; Kretinin, A. V.; Chen, Y.; Giannini, V.; Fogler, M. M.; Francescato, Y.; Ellis, C. T.; Tischler, J. G.; Woods, C. R.; Giles, A. J.; et al. Sub-Diffractional Volume-Confined Polaritons in the Natural Hyperbolic Material Hexagonal Boron Nitride. *Nat. Commun.* **2014**, *5*, 5221.

(10) Korzeb, K.; Gajc, M.; Pawlak, D. A. Compendium of Natural Hyperbolic Materials. *Opt. Express* **2015**, *23*, 25406.

(11) Sun, J.; Litchinitser, N. M.; Zhou, J. Indefinite by Nature: From Ultraviolet to Terahertz. *ACS Photonics*. **2014**, *1*, 293–303.

(12) Avrutsky, I.; Salakhutdinov, I.; Elser, J.; Podolskiy, V. Highly Confined Optical Modes in Nanoscale Metal-Dielectric Multilayers. *Phys. Rev. B* **2007**, *75*, 241402(R).

(13) Ishii, S.; Kildishev, A. V.; Narimanov, E.; Shalaev, V. M.; Drachev, V. P. Sub-Wavelength Interference Pattern from Volume Plasmon Polaritons in a Hyperbolic Medium. *Laser Photonics Rev.* **2013**, *7*, 265–271.

(14) Zhukovsky, S. V; Kidwai, O.; Sipe, J. E. Physical Nature of Volume Plasmon Polaritons in Hyperbolic Metamaterials. *Opt. Express* **2013**, *21*, 14982–14987.

(15) Sreekanth, K. V.; De Luca, A.; Strangi, G. Experimental Demonstration of Surface and Bulk Plasmon Polaritons in Hypergratings. *Sci. Rep.* **2013**, *3*, 3291.

(16) Sreekanth, K. V; De Luca, A.; Strangi, G. Excitation of Volume Plasmon Polaritons in Metal-Dielectric Metamaterials Using 1D and 2D Diffraction Gratings. *J. Opt.* **2014**, *16*, 105103.
(17) Sreekanth, K. V.; Alapan, Y.; ElKabbash, M.; Ilker, E.; Hinczewski, M.; Gurkan, U. A.; De Luca, A.; Strangi, G. Extreme Sensitivity Biosensing Platform Based on Hyperbolic Metamaterials. *Nat. Mater.* **2016**, *15*, 4–11.
(18) Feng, K.; Harden, G.; Sivco, D. L.; Hoffman, A. J. Subdiffraction Confinement in All-Semiconductor Hyperbolic Metamaterial Resonators. *ACS Photonics* **2017**, *4*, 1621–1626.
(19) Feng, K.; Sivco, D. L.; Hoffman, A. J. Engineering Optical Emission in Sub-Diffraction Hyperbolic Metamaterial Resonators. *Opt. Express* **2018**, *26*, 4382.
(20) Law, S.; Liu, R.; Wasserman, D. Doped Semiconductors with Band-Edge Plasma Frequencies. *J. Vac. Sci. Technol. B* **2014**, *32*, 052601.
(21) Law, S.; Yu, L.; Wasserman, D. Epitaxial Growth of Engineered Metals for Mid-Infrared Plasmonics. *J. Vac. Sci. Technol. B* **2013**, *31*, 03C121.
(22) Hoffman, A. J.; Alekseyev, L.; Howard, S. S.; Franz, K. J.; Wasserman, D.; Podolskiy, V. A.; Narimanov, E. E.; Sivco, D. L.; Gmachl, C. Negative Refraction in Semiconductor Metamaterials. *Nat. Mater.* **2007**, *6*, 946–950.
(23) Wei, D.; Harris, C.; Bomberger, C. C.; Zhang, J.; Zide, J.; Law, S. Single-Material Semiconductor Hyperbolic Metamaterials. *Opt. Express* **2016**, *24*, 8735–8745.
(24) Shekhar, P.; Jacob, Z. Strong Coupling in Hyperbolic Metamaterials. *Phys. Rev. B* **2014**, *90*, 045313.
(25) Law, S.; Adams, D. C.; Taylor, A. M.; Wasserman, D. Mid-Infrared Designer Metals. *Opt. Express* **2012**, *20*, 12155–12165.
(26) Wei, D.; Harris, C.; Law, S. Volume Plasmon Polaritons in Semiconductor Hyperbolic Metamaterials. *Opt. Mater. Express* **2017**, *7*, 2672–2681.
(27) Basu, P. K.; Nag, B. R. Estimation of Alloy Scattering Potential in Ternaries from the Study of Two-Dimensional Electron Transport. *Appl. Phys. Lett.* **1983**, *43*, 689–691.
(28) Basu, P. K.; Nag, B. R. Alloy Scattering Limited Mobility of Two Dimensional Electron Gas Formed in In0.53Ga0.47As. *Surf. Sci.* **1984**, *142*, 256–259.
(29) Huang, S. H.; Balakrishnan, G.; Khoshakhlagh, A.; Jallipalli, A.; Dawson, L. R.; Huffaker, D. L. Strain Relief by Periodic Misfit Arrays for Low Defect Density GaSb on GaAs. *Appl. Phys. Lett.* **2006**, *88*, 131911.

For Table of Contents Use Only

Simultaneous large mode index and high quality factor in infrared hyperbolic metamaterials

Patrick Sohr,[1†] Dongxia Wei,[1†] Stephanie Tomasulo,[2] Michael K. Yakes,[2] and Stephanie Law[1*]

[1] Department of Materials Science and Engineering, University of Delaware, Newark, Delaware 19702, United States

[2] Naval Research Laboratory, 4555 Overlook Ave. SW, Washington, DC 20375, United States

[*]corresponding author: slaw@udel.edu

[†] Patrick Sohr and Dongxia Wei contributed equally

The left hand panel of this graphic is a schematic of our hyperbolic metamaterial structure. The right three panels are simulations of the mode profiles of the volume plasmon polariton modes excited within the metamaterial.